Int. J. Therm. Sci. (2000) 39, 85–95

S1290-0729(00)00193-8/FLA

Frost deposition in a parallel plate channel under laminar flow conditions

Andreas Lüer, Hans Beer *

Institut für Technische Thermodynamik, Technische Universität Darmstadt, Petersenstraße 30, 64287 Darmstadt, Germany

(Received 19 January 1999, accepted 18 May 1999)

Abstract — The subject of this paper is a theoretical and experimental study of frost formation on cooled parallel plates in laminar forced convection. In the experiments time variation of the frost layer thickness was measured at several locations downstream along the test section which was positioned in an open-loop wind tunnel. The parameters varied were air velocity (Reynolds number), air temperature, air humidity ratio, and plate temperature. The process was simulated numerically using a two-dimensional transient model based on the conservation equations of mass, momentum, energy, and species. The physical domain of interest was divided into two subdomains, one for the moist air stream between the plates (gaseous phase), and one for the frost layer (solid phase). The two sets of governing equations were coupled by boundary conditions at the moving interface which required an iterative solution strategy. With this approach, the local distribution of temperature and porosity in the frost layer, which is nearly impossible to obtain in the experiments, could be predicted at any time. The results of the total heat and mass transfer rates as well as the development of the local and average frost thicknesses were compared with the experimental findings. © 2000 Éditions scientifiques et médicales Elsevier SAS

frost / humid air / laminar forced convection / coupled heat and mass transfer / parallel plates / growth / porosity / densification / numerical simulation / moving boundary / SIMPLER

Nomenclature

b	breadth	b^*/d^*
$x,\ y$	Cartesian coordinates	$x^*/d^*,\ y^*/d^*$
d^*	diameter (hydraulic)	$(2b^*z^*)/(b^*+z^*)$ [m]
D	diffusion coefficient	D^*/D_0^*
h	enthalpy	h^*/h_{sg}^*
c	heat capacity (specific)	c^*/c_0^*
z	height	z^*/d^*
$\boldsymbol{n}$	normal vector	
Pr	Prandtl number	$(\rho_0^*\upsilon_0^*c_0^*)/\lambda_0^*$
p	pressure	$p^*/(\rho_0^*\bar{u}_0^{*2})$
Re_{d}	Reynolds number	$(\bar{u}_0^*d^*)/\upsilon_0^*$
Sc_{b}	Schmidt number (bulk)	$\upsilon_0^*/D_{\mathrm{VA0}}^*$
Sc_{f}	Schmidt number (frost)	$(\upsilon_0^*\rho_0^*(\rho_{\mathrm{P}}^*-\rho_{\mathrm{Vf}}^*))/(D_{\mathrm{f}}^*\rho_{\mathrm{P}}^{*2})$
Ste	Stefan number	$(c_0^*(T_0^*-T_{\mathrm{w}}^*))/h_{\mathrm{sg}}^*$
$T^*,\ T_{\mathrm{c}}^*$	temperature	K, °C
t	time	$(t^*\bar{u}_0^*)/d^*$
$u,\ v$	velocities	$u^*/\bar{u}_0^*,\ v^*/\bar{u}_0^*$
$\boldsymbol{u}$	velocity vector	

Greek symbols

ρ	density	ρ^*/ρ_0^*
μ	diffusion resistance factor	τ/ε
δ	free channel height	δ^*/d^*
$\dot{\boldsymbol{\delta}}$	vertical frost surface velocity vector	
ε	porosity	$(\rho_{\mathrm{I}}-\rho_{\mathrm{f}})/(\rho_{\mathrm{I}}-\rho_{\mathrm{P}})$
θ	temperature	$(T^*-T_{\mathrm{m}}^*)/(T_0^*-T_{\mathrm{w}}^*)$
λ	thermal conductivity	λ^*/λ_0^*
τ	tortuosity	
υ	viscosity (kinematic)	υ^*/υ_0^*
φ	relative humidity	%

Subscripts

A	air (dry)
c	Celsius
$x,\ y$	derivative relating to
d	diameter (hydraulic)
dyn	dynamic
0	entrance and at time zero
f	frost
g	gas stream of humid air
I	ice
m	melting point

* Correspondence and reprints.
df5j@hrzpub.tu-darmstadt.de

P pores
sg sublimation
s surface of the frost layer
V vapour
w wall

Superscripts

– average value
∗ quantity in SI units
′ saturated

1. INTRODUCTION

When a cold surface with temperature below the dew point of water vapour is exposed to humid air, moisture will condense. If additionally the surface temperature is below the freezing point, frost formation will occur. In most industrial applications (e.g., heat exchangers) this phenomenon is undesirable because of the insulating effect of the frost layer along with the reduction in heat transfer and because of the decrease in airflow area which entails an increase in pressure loss.

Frost formation has been investigated for over 65 years so that the available literature is fairly extensive. In the beginning, studies mainly concentrated on the experimental observation of frost growing under free and forced convection in simple geometries, e.g., flat plates [1] or circular cylinders [2], and heat exchangers [3]—a literature review is given by O'Neal and Tree [4] and Padki et al. [5], for example. A thorough examination of the existing literature reveals that little work is done on frost formation between parallel plates in laminar forced convection. In most experiments only one of the two plates is held at constant temperature [6, 7] or a streamwise linearly decreasing temperature distribution is used [8]. In the study presented both plates are kept at constant temperature, and the air stream is entering the test section with a developed laminar velocity profile.

In any case the incipient frost development is characterised by the formation of subcooled water droplets. When the droplets reach a certain size, they freeze abruptly and ice crystals begin to grow [9]. According to Hayashi et al. [10] the formation of frost can be subdivided into three periods: "crystal growth period", "frost layer growth period", and "frost layer full growth period". When the frost layer develops it passes these periods, and the crystal growth changes from one-dimensional to three-dimensional, entailing a densification of the frost layer. The thickness and the surface temperature of the frost increase until the melting temperature of water (0 °C) is reached. Then liquid water forms on the surface due to the melting of ice crystals and to condensation of vapour from the humid air—in literature this phenomenon is called "meltback". The water soaks into the frost layers, where it freezes and the rise in density reduces the thermal resistance of the porous layer so that the surface temperature drops and subsequently crystals of ice can grow on top of the existing layer again. This cyclic behaviour characterizes the "frost layer full growth period".

The shape of the frost not only depends on time, but also on the prevailing conditions under which it is formed. Of great influence are the air velocity, air temperature, air humidity and cold plate temperature—as will be discussed in detail in section 4. Hayashi et al. [10], for example, distinguish between four types of crystals. The spectrum reaches from a more feather-like to a plate-like appearance, depending on the concentration difference between the main stream and the frost surface.

Generally speaking, the experimental findings help to better understand the process of frost formation, but in particular they enable the verification of theoretical investigations. At first, analytical models based on a heat and a mass balance between the humid air and the frost surface were developed to predict the change of thickness, density, and surface temperature. Empirical correlations were used to deal with the convective transfer to the frost surface, while diffusion was supposed to be the dominant transport mechanism in the interior of the porous layer [11, 12]. Usually, local variations of the frost thickness were not considered. Although the presented models deliver satisfactory results concerning the overall behaviour of the frost, these approaches suffer from one fundamental disadvantage. They are not able to predict the spatial temperature and porosity distribution inside the frost. Tao et al. [13] were among the first to incorporate the conservation equations of heat and mass for the frost layer to remedy this drawback.

In this study an even more rigorous mathematical model is presented, solving not only the governing equations of the frost regime but also the conservation equations of heat and mass for the humid air. The numerical method is used to simulate the frost formation on cooled parallel plates in laminar forced convection. The theoretical results are compared with the experimental findings to demonstrate the capabilities of the developed model on the one hand and to reveal its shortcomings on the other hand.

2. MEASUREMENT METHOD

In order to investigate the influence of the four major parameters on frost formation: Reynolds number, relative

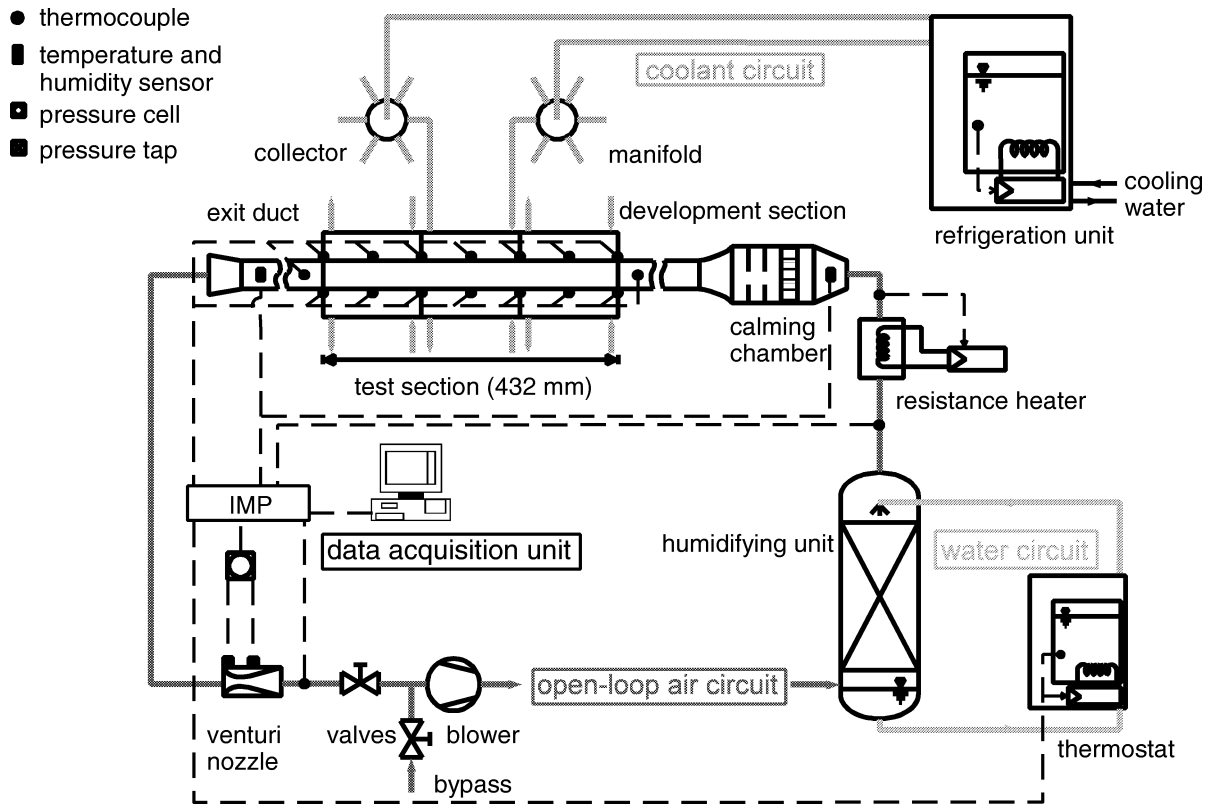

Figure 1. Scheme of the experimental apparatus.

TABLE I
Test conditions.

Parameter	Operating range
Reynolds number	700–2 300
Relative humidity	40–90 %
Air temperature	12–30 °C
Wall temperature	−16–−2 °C

humidity, air temperature, and wall temperature, a test rig was constructed. The range of influence parameters covered is given in *table I*.

The experimental setup (*figure 1*) consists of three circuits: air (primary) circuit, coolant (secondary) circuit, and water (tertiary) circuit. Of primary interest is the open-loop wind tunnel with the installed test section. Before the air reaches the parallel plate channel, it has to undergo several manipulations to obtain the desired entrance conditions. At first, the air passes the humidifying section in countercurrent to the water of the tertiary circuit. The water entrance temperature in the packed column is kept constant with the help of a thermostat. The air gets nearly saturated at the given water temperature and, therefore, subsequently is heated to the desired temperature level by an electric resistance heater. Both, the humidity and the temperature are measured by a sensor (VAISALA: HMP 233A80) before entering the straightening section. The calming chamber consists of a honeycomb and two wire mesh screens and is connected to a nozzle. Finally, the air passes a 6 m long duct of rectangular cross-section to ensure a fully developed velocity profile at the entrance of the test section. A 1 m long exit duct is mounted behind, where the air temperature and humidity are measured again. The flow rate is metered using a calibrated venturi nozzle and a pressure cell. Two control valves, one for the main air stream and one for the bypass stream, allow the adjustment of the desired air flow or Reynolds number, respectively. The centrifugal blower is arranged at the end of the wind tunnel in order not to disturb the air stream in any way. The piping is encased with polystyrene foam and glass wool to prevent heat exchange with its surroundings. The signals of the temperature, humidity, and pressure sensors are recorded

by a data acquisition unit so that they are available for later analyses.

The 114 mm wide, 24 mm high, and 432 mm long test section is formed by two horizontally arranged aluminium plates and two transparent polycarbonat walls, which are bolt at the sides. To keep the aluminium surface at the desired temperature, a solution of ethylene glycol and water circulates between the test section and a refrigeration unit (secondary circuit). Each aluminium plate is divided into three independently supplied chambers to achieve a temperature distribution as homogeneous as possible (axial deviation less then ± 0.2 K). The wall temperature is monitored by 2×7 equally spaced thermocouples (chromel/alumel) embedded in the cooled plates.

Since the side walls of the test section are transparent, the process of frost formation can easily be observed and the local frost thickness can be determined, respectively. Using a microscope with an inserted scale the achieved measurement accuracy is ± 0.1 mm. When running a test of 4 hours duration the local frost layer thickness is measured every 30 min and photographs are taken additionally. With it, the average density of the frost can be calculated, when the rate of water condensing out of the humid air stream is measured. Besides, the latent and sensible energy rates transferred to the cold plates are provided by the experiments.

3. MATHEMATICAL DEVELOPMENT

A two-dimensional transient numerical model, based on the conservation equations of mass, momentum, energy and species, is derived, to investigate the frost formation between parallel plates theoretically. The physical domain of interest is divided into two subdomains, one for the humid air and one for the frost layer (*figure 2*). They are connected by the moving interface and coupled by their heat and mass exchange. Obviously, the process of frost growth is too complex to be simulated with all its

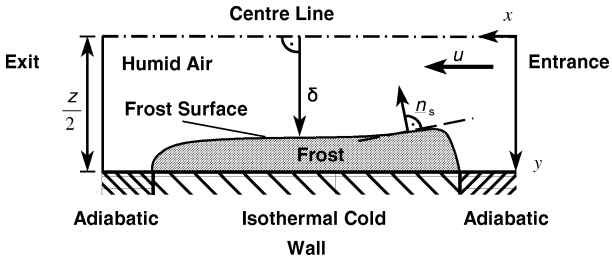

Figure 2. Physical domain.

effects. Some simplifications have to be made, the major assumptions for the gas stream of moist air are: constant properties, gravitational effects are negligible so that the problem is symmetric to the middle axis of the test section, Newton fluid, Fourier's law is valid, and the roughness of the frost surface does not have any influence.

Moreover, the following assumptions are made for the porous frost layer: constant total pressure of the gaseous phase, humid air in the porous layer is saturated and a mixture of ideal gases, local thermal equilibrium, Fick's law and Fourier's law are valid, Soret effect and Dufour effect are negligible, and convection and radiation are negligible.

For simplicity, the values of dry air at entrance conditions are assumed to represent the properties of the humid air stream. They can be obtained from standard tables, e.g., VDI-Wärmeatlas [14]. The density of the frost layer is calculated from its component values as a volume average, the specific heat capacity as a mass average. When diffusion in a porous layer is modelled according to Fick's law, a diffusion resistance factor μ, expressed by the ratio of tortuosity τ to porosity ε, has to be introduced to account for the changing effective cross sectional area. The thermal conductivity of frost is related to the density in first place. Several empirical correlations and theoretical equations can be found in the literature. The former often suffer from a limited range of applicability, so that a more general relationship based on a structure model should be preferred. Both, the binary diffusion coefficient and the tortuosity as well as the frost thermal conductivity are implemented according to Auracher [15].

Considering the aforementioned points the governing equations in nondimensional form are:

$$\nabla \cdot \boldsymbol{u} = 0 \tag{1}$$

$$\frac{\partial \boldsymbol{u}}{\partial t} + \nabla \cdot (\boldsymbol{u}\boldsymbol{u}) = -\nabla p_{\mathrm{dyn}} + \frac{1}{Re_{\mathrm{d}}} \Delta \boldsymbol{u} \tag{2}$$

$$\frac{\partial \rho_{\mathrm{Vg}}}{\partial t} + \nabla \cdot (\rho_{\mathrm{Vg}} \boldsymbol{u}) = \frac{1}{Re_{\mathrm{d}} Sc_{\mathrm{g}}} \Delta \rho_{\mathrm{Vg}} \tag{3}$$

$$\frac{\partial \theta_{\mathrm{g}}}{\partial t} + \nabla \cdot (\theta_{\mathrm{g}} \boldsymbol{u}) = \frac{1}{Re_{\mathrm{d}} Pr} \Delta \theta_{\mathrm{g}} \tag{4}$$

$$\frac{\partial ((1-\varepsilon)\rho_{\mathrm{I}})}{\partial t} + \frac{\partial (\varepsilon \rho_{\mathrm{Vf}})}{\partial t} = \frac{1}{Re_{\mathrm{d}}} \nabla \cdot \left(\frac{\varepsilon}{Sc_{\mathrm{f}}} \nabla \left(\frac{\rho_{\mathrm{Vf}}}{\rho_{\mathrm{P}}} \right) \right) \tag{5}$$

$$\rho_{\mathrm{f}} c_{\mathrm{f}} \frac{\partial \theta_{\mathrm{f}}}{\partial t} = \frac{1}{Re_{\mathrm{d}} Pr} \nabla \cdot (\lambda_{\mathrm{f}} \nabla \theta_{\mathrm{f}}) + \frac{1}{Ste} \frac{\partial ((1-\varepsilon)\rho_{\mathrm{I}})}{\partial t} \tag{6}$$

The porosity and the density of the pores are defined as

$$\varepsilon = \frac{\rho_\mathrm{I} - \rho_\mathrm{f}}{\rho_\mathrm{I} - \rho_\mathrm{P}} \quad \text{and} \quad \rho_\mathrm{P} = \rho_\mathrm{Vf} + \rho_\mathrm{A} \tag{7}$$

To solve the system of transient elliptic equations, initial conditions for all dependent variables and boundary conditions on every edge of the physical domain are necessary (*figure 2*). Special treatment of the moving interface between the two subdomains is required. The boundary conditions in nondimensional form are:

Entrance:

$$\begin{aligned} u &= \frac{3}{2}\left(1 - \left(\frac{2y}{z}\right)^2\right) \\ v &= 0, \qquad \rho_\mathrm{Vg} = \rho_0, \qquad \theta_\mathrm{g} = \theta_0 \end{aligned} \tag{8}$$

Exit:

$$\frac{\partial u}{\partial x} = \frac{\partial v}{\partial x} = \frac{\partial \rho_\mathrm{Vg}}{\partial x} = \frac{\partial \theta_\mathrm{g}}{\partial x} = 0 \tag{9}$$

Centre line:

$$\frac{\partial u}{\partial y} = v = \frac{\partial \rho_\mathrm{Vg}}{\partial y} = \frac{\partial \theta_\mathrm{g}}{\partial y} = 0 \tag{10}$$

Wall:

$$\begin{aligned} u = v &= \frac{\partial \rho_\mathrm{Vg}}{\partial y} = \frac{\partial \theta_\mathrm{g}}{\partial y} = 0 \\ \varepsilon &= 0, \qquad \rho_\mathrm{Vf} = \rho_\mathrm{V}'(\theta_\mathrm{w}), \qquad \theta_\mathrm{f} = \theta_\mathrm{w} \end{aligned} \tag{11}$$

The coupling conditions contain the mass and the energy balance at the frost surface. Besides, they express that the dependent variables u, v, ρ, θ for the two numerical regimes must be equal at the joint boundary—the frost surface:

$$\begin{aligned} & u = -\delta_x v, \qquad v = \frac{1-\varepsilon}{1+\delta_x^2}\dot{\delta}, \qquad \theta_\mathrm{g} = \theta_\mathrm{f} = \theta_\mathrm{s} \\ & \rho_\mathrm{Vg} = \rho_\mathrm{Vf} = \rho_\mathrm{Vs} = \rho_\mathrm{V}'(\theta_\mathrm{s}), \qquad \varepsilon = \varepsilon_\mathrm{s}(x) \\ & \left(-\nabla\theta_\mathrm{g} + \lambda_\mathrm{f}\nabla\theta_\mathrm{f} - \frac{Re_\mathrm{d}Pr}{Ste}(1-\varepsilon)\rho_\mathrm{I}\dot{\boldsymbol{\delta}}\right)\cdot \boldsymbol{n}_\mathrm{s} = 0 \\ & \left(-\nabla\rho_\mathrm{Vg} + \frac{Sc_\mathrm{g}}{Sc_\mathrm{f}}\varepsilon\nabla\left(\frac{\rho_\mathrm{Vf}}{\rho_\mathrm{P}}\right)\right)\cdot \boldsymbol{n}_\mathrm{s} \\ & \quad + \left(Re_\mathrm{d}Sc_\mathrm{g}(1-\varepsilon)\rho_\mathrm{I}\dot{\boldsymbol{\delta}}\right)\cdot \boldsymbol{n}_\mathrm{s} = 0 \end{aligned} \tag{12}$$

For the humid air domain the initial values correspond to the prevailing conditions at the entrance. For the frost regime the porosity distribution at the surface and the cold wall temperature are used as initial values. The surface porosity ε_s has to be chosen reasonably to allow the best possible correspondence between the numerical and experimental results (see next section). To immobilize the frost surface in the numerical domain the model equations are transformed from a Cartesian to a contour fitted coordinate system.

The next task is to develop a computational procedure that enables the desired numerical solution. First, the discrete forms of equations (1)–(12) are derived by applying the finite-volume method. Based on exponential equations the spatial grid is generated algebraically so that regions of steeper gradients can easily be taken into account by grid refinement. The governing equations are solved one after the other using the MSIP algorithm of Schneider and Zedan [16]. An iterative procedure is required to match the solutions of the single equations for each time step, since they are coupled. Here, the SIMPLER algorithm of Patankar [17] is adopted. Starting with a very small uniform thickness the transient shape of the frost layer can now be calculated step by step. It is of particular importance to choose a step size small enough, to avoid any effect on the results. The simulation program stops either when the triple point temperature of water is reached (beginning of "meltback") or the duration of the experiments is exceeded.

4. EXPERIMENTAL AND NUMERICAL RESULTS

Although most of the parameter combinations run in the experiments have been simulated, only the variation of Reynolds number, humidity, air temperature, and wall temperature are presented for a comparison. Before that, some general findings shall be discussed.

One major outcome of the experiments was the development of the frost thickness. In *figure 3* a typical frost layer after 3 hours is shown, whereby the humid air passes the test section from right to left. As can be seen, a layer of almost constant thickness—apart from the leading and trailing edge—has formed. Keeping in mind the streamwise rapidly decreasing local mass flow to the surface (*figure 4*), however, one would expect a frost contour appearing fairly similar. A look at *figure 5*, where the frost contour is depicted at different times, gives an idea of how complex the process of frost formation with its various mechanisms of heat and mass transfer involved really is. At the beginning of the experiment the thickness falls off according to the streamwise reduction in mass transfer, but it is nearly constant after 2 hours. This is an indication, that an excessive densification (through diffusion and "meltback"-effect) takes place near the leading

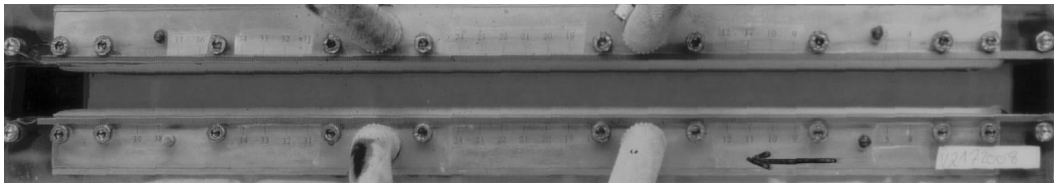

Figure 3. Photograph of the frost layer after 3 hours ($Re_d = 2\,100$, $\varphi_0 = 70\,\%$, $T^*_{c,0} = 20\,°C$, $T^*_{c,w} = -8\,°C$).

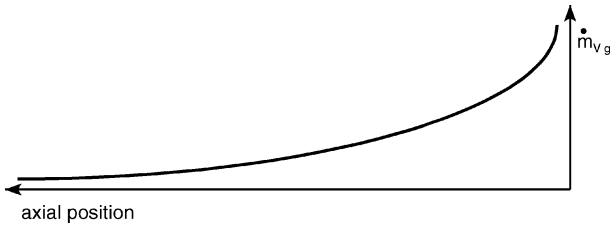

Figure 4. Local mass transfer as function of axial position.

edge, while the frost porosity increases in the streamwise direction. At the end of the experiment a slight gradient in thickness can be observed again. As mentioned already, this cyclic behaviour is typical for the "frost layer full growth period".

Besides, from the diminishing distances between the curves in *figure 5* it can be deduced that the average frost height rises quickly at the beginning, but the growth rate levels off later on. Since the overall mass transfer to the surface is almost constant in time, the average frost density gradually increases.

As the numerical simulations have shown, the porosity distribution at the frost surface, which is the only parameter left to alter in the model, is crucial for the theoretical predictions as well. But the scope for variations is very limited. The choice made for the surface porosity is a result of an iterative process of the interaction between assumptions and numerical results. According to this finding the porosity continuously increases from zero at the front edge of the frost layer to a value around 0.95, which is retained for most of the plate length (*figure 6* for an example). Only at the rear end the porosity quickly drops off to zero, again [18].

Figure 7 shows the temperature and the porosity distribution inside the frost layer. The lines of constant temperature are aligned almost horizontally so that the point of highest temperature is located on the surface at an axial position, where the frost layer reaches its maximum. However, the highest density appears at the front edge next to the cold wall. The density not only decreases in the axial direction but also towards the surface.

4.1. Variation of Reynolds number

The overall mass transfer to the frost surface increases with increasing Reynolds number, which affects both, the average density and the thickness. Comparing frost contours at the same time but different air speeds reveals that a higher Reynolds number basically causes a more homogeneous frost layer with the leading edge thickness remaining almost constant and the downstream height increasing.

While in the simulation the effect on thickness is slightly more pronounced, in the experiment the changes in density seem to dominate, leading to a less definite dependence on Re_d. In *figure 8*, the predicted and measured average frost heights versus time are depicted. The higher the Reynolds number, the faster the thickness increases and the sooner the simulation stops, because the surface temperature exceeds the triple point of water. This obviously is due to a too weak densification which increases the thermal resistance and herewith the surface temperature. Apart from that, the decline of the frost growth rate with time can also be seen in *figure 8*. For comparison, one test with turbulent air flow ($Re_d = 5\,000$) is added. Although no turbulence model is implemented, the numerical approach delivers satisfactory results.

The impact of the Reynolds number on heat transfer is double, since both the sensible and the latent component are affected. Their shares in the overall energy transfer to the cold plate are of the same order of magnitude [18].

4.2. Variation of humidity

A change in the relative humidity of the gas stream does not have any effect on the dimensionless quantities like Re_d or Sc_b, but influences the prevailing gradient in the concentration boundary layer. Therefore, the mass

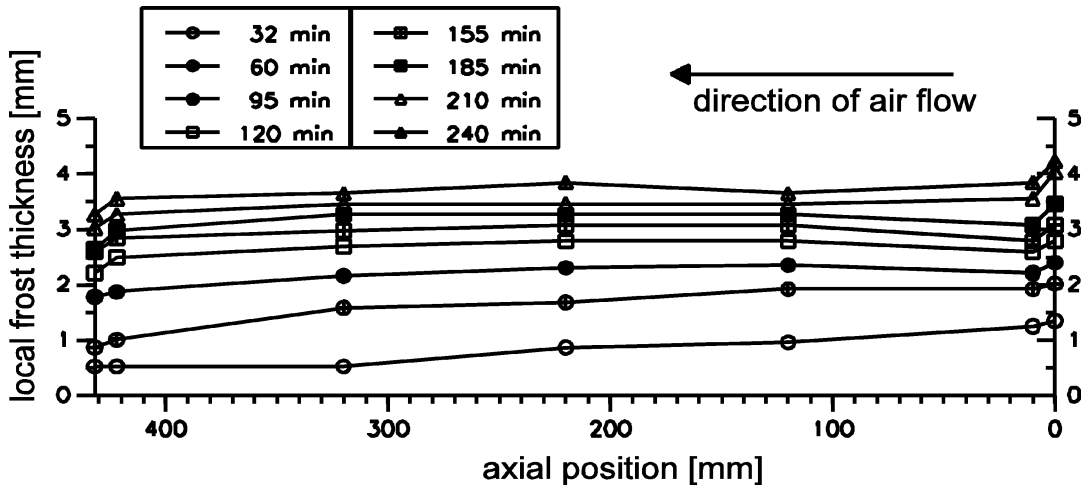

Figure 5. Measured frost thickness at different times ($Re_d = 1\,500,\ \varphi_0 = 70\,\%,\ T^*_{c,0} = 20\,°C,\ T^*_{c,w} = -8\,°C$).

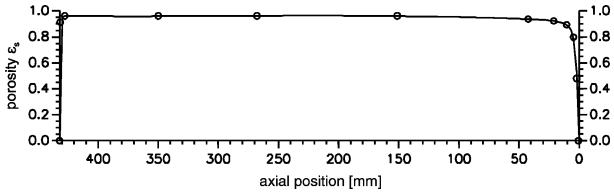

Figure 6. Assumed porosity distribution at the frost surface ($Re_d = 1\,500,\ \varphi_0 = 70\,\%,\ T^*_{c,0} = 20\,°C,\ T^*_{c,w} = -8\,°C$).

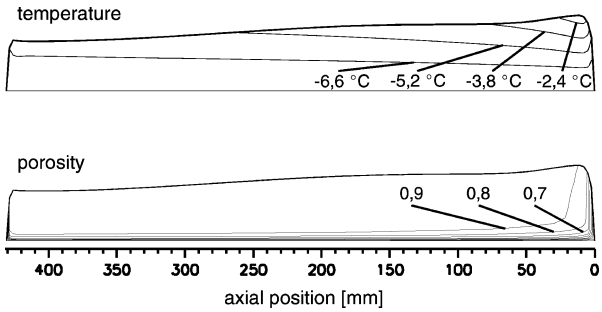

Figure 7. Predicted temperature and porosity distribution inside the frost layer after 32 minutes ($Re_d = 1\,500,\ \varphi_0 = 70\,\%,\ T^*_{c,0} = 20\,°C,\ T^*_{c,w} = -8\,°C$).

transfer to the frost layer increases with growing relative humidity and so does the growth rate. As can be seen in *figure 9*, the correspondence between the measured and the predicted time variation of the average thickness is quite good. Again, a fast growing frost layer results in a short simulation time, until the local surface temperature reaches 0 °C.

For a relative humidity of 60 %, the frost contours at different times are shown in *figure 10*. The agreement between the experimental and theoretical results is satisfactory, although some differences exist. While the predicted height of the maximum at the front edge is consistent with the measurement, the decrease in the streamwise direction is less pronounced in the simulation.

The concentration difference between the air flow and the frost surface also affects the structure of the growing frost as already mentioned (see also Hayashi et al. [10]). For the parameter combinations considered, mainly plate-like crystals develop. Altogether, the time variation of the average density with varying relative humidity is quite complex (*figure 11*). In the initial phase, before "meltback" occurs, frost forms with low density when the water content of the air flow is large and vice versa. While at low humidity the density decreases at first, at high humidity it always increases. The greater the amount of water available the faster the density grows so that in long term the density behaves proportional to the humidity.

Since the sensible heat transfer is almost unaffected by growing humidity, the overall heat flux increases due to its increasing latent component [18].

4.3. Variation of air temperature

Investigating the effect of air inlet temperature on frost formation two different cases are considered.

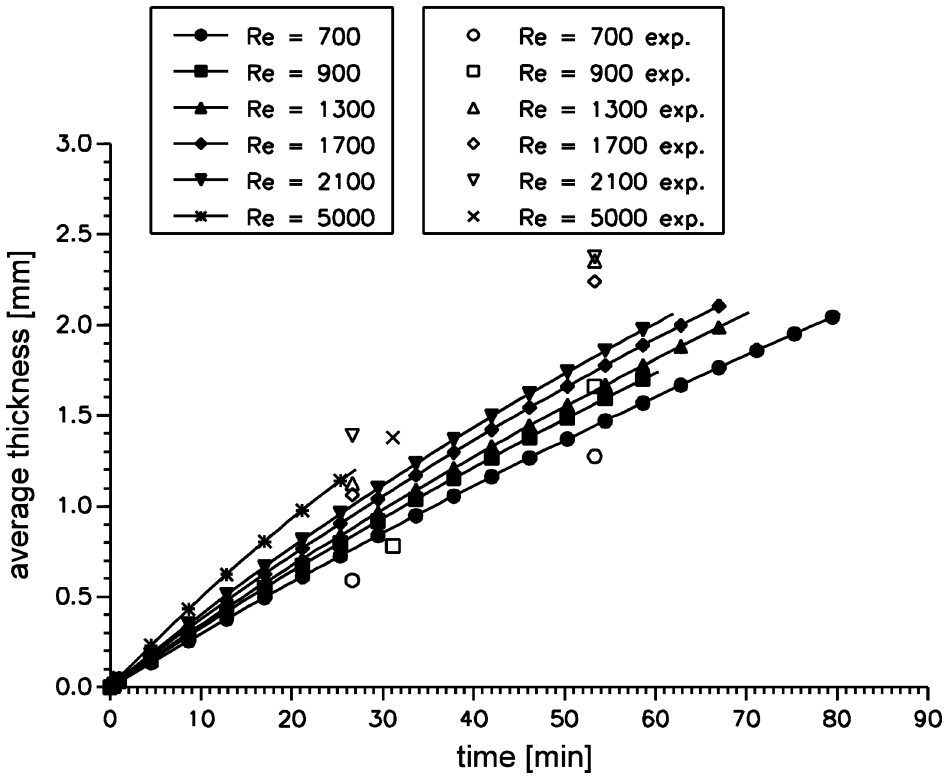

Figure 8. Average frost thickness versus time with varying Reynolds numbers ($\varphi_0 = 70\,\%,\ T^*_{c,0} = 20\,°C,\ T^*_{c,w} = -8\,°C$).

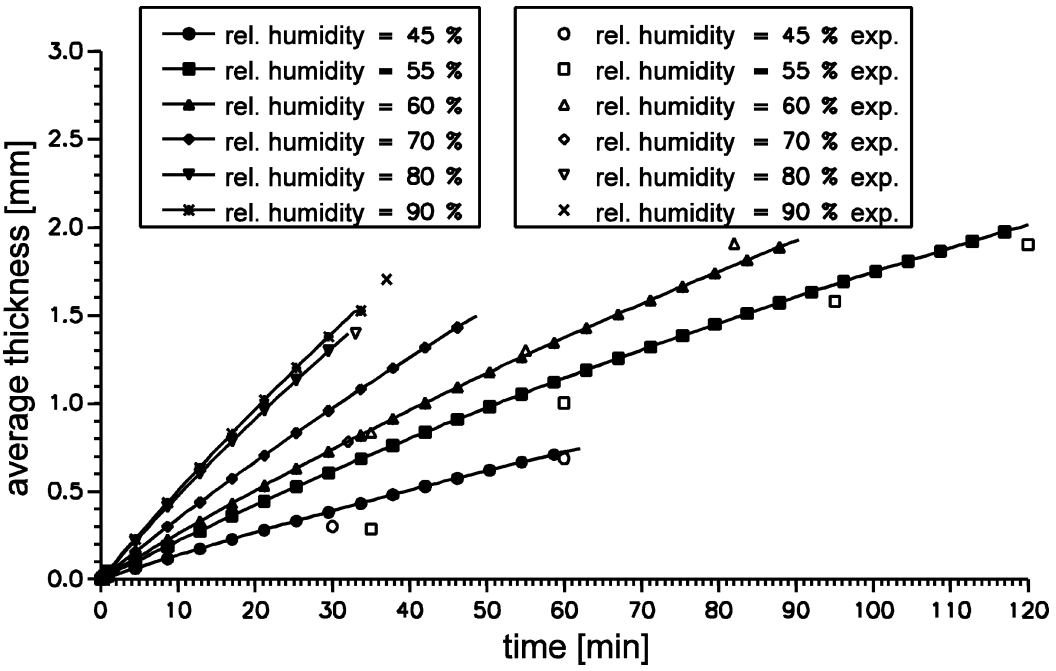

Figure 9. Average frost thickness versus time with varying relative humidity ($Re_d = 1\,500,\ T^*_{c,0} = 20\,°C,\ T^*_{c,w} = -8\,°C$).

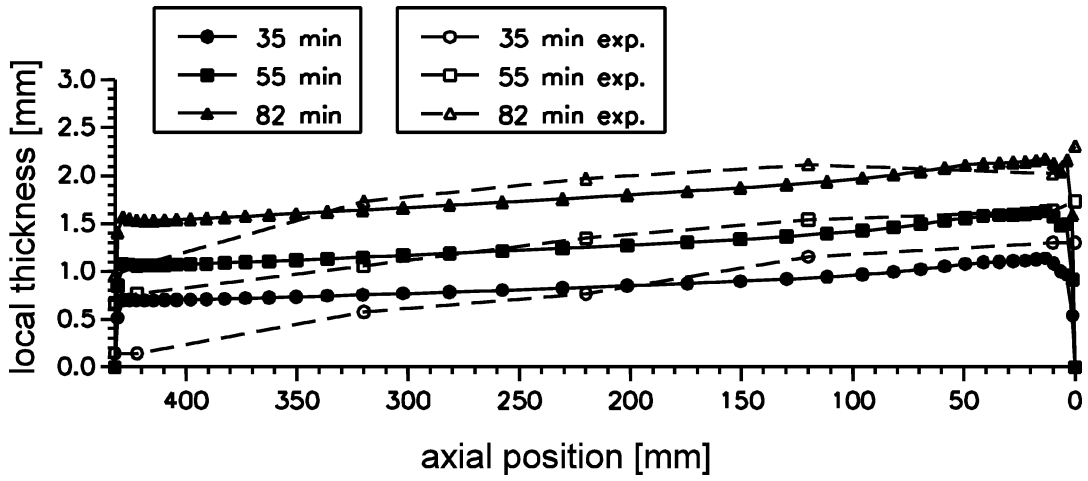

Figure 10. Time variation of local frost thickness ($Re_d = 1500$, $\varphi_0 = 60\,\%$, $T^*_{c,0} = 20\,°C$, $T^*_{c,w} = -8\,°C$).

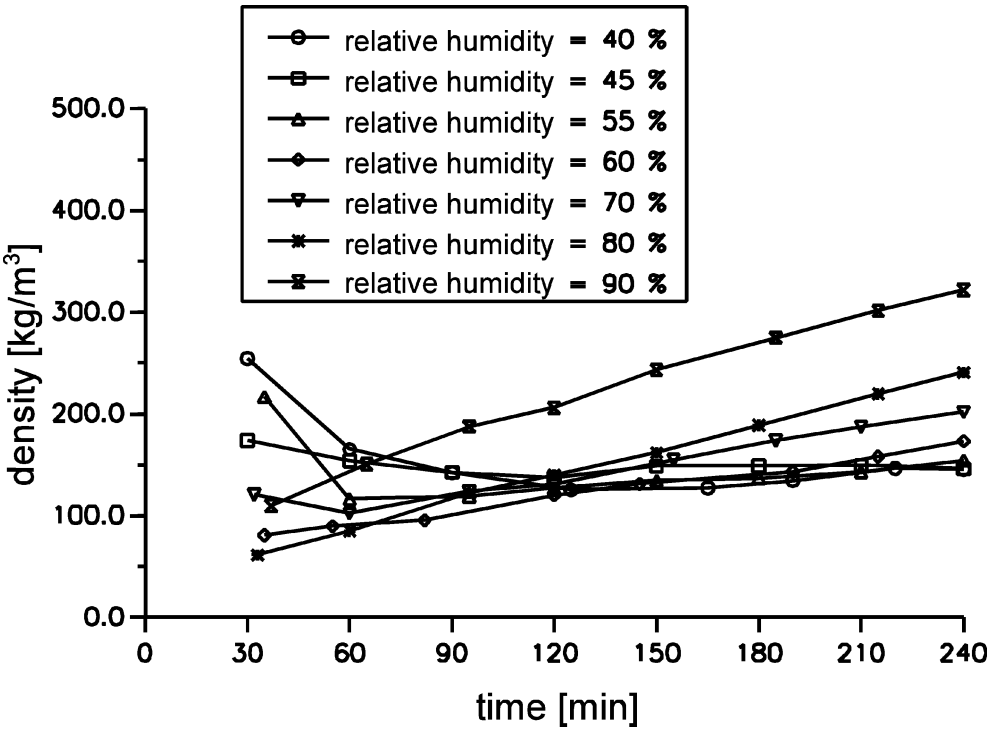

Figure 11. Measured average frost density with varying relative humidity ($Re_d = 1500$, $T^*_{c,0} = 20\,°C$, $T^*_{c,w} = -8\,°C$).

In the first case the relative humidity is held constant at 70 %. Hence, a change of air temperature always comes along with a change of water content, so that both convective heat and mass transfer are affected. Increasing the air temperature from 12 °C to 28 °C triples the average mass flux to the frost surface and almost doubles the heat flux. The increase in heat transfer is mainly caused by the enhanced release of its latent component, whereas the sensible component does not change very much. The results look quite similar to the outcome for the variation of humidity as described in the previous section. Therefore, it is interesting to see

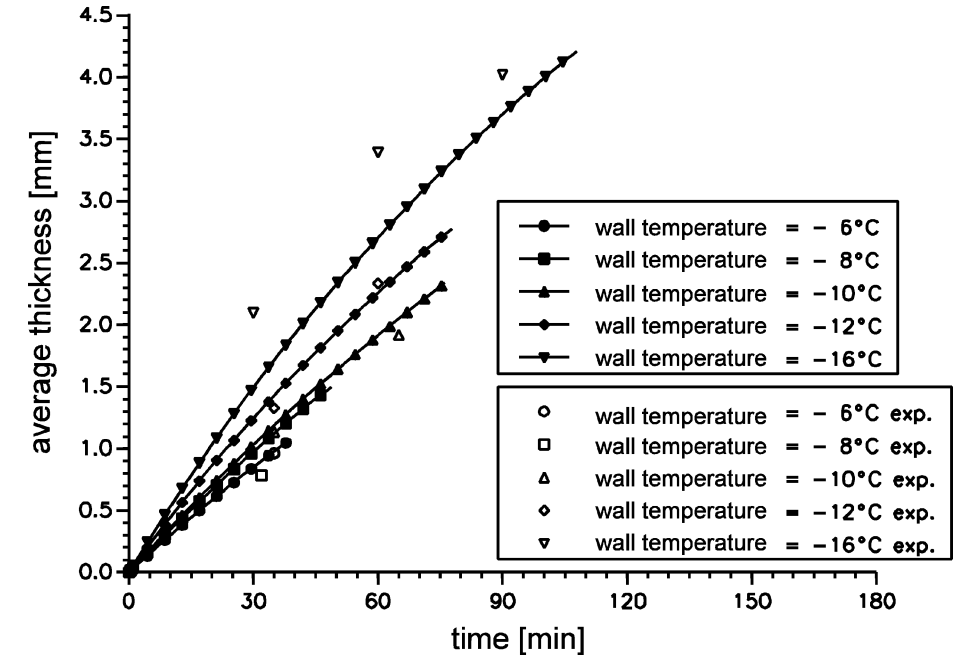

Figure 12. Average frost thickness versus time with varying wall temperature ($Re_d = 1\,500,\ \varphi_0 = 70\,\%,\ T^*_{c,0} = 20\,°C$).

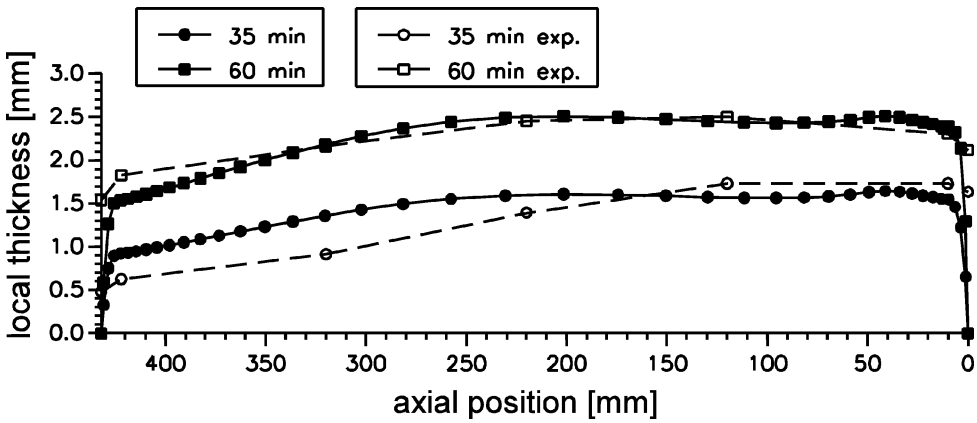

Figure 13. Time variation of local frost thickness ($Re_d = 1\,500,\ \varphi_0 = 70\,\%,\ T^*_{c,0} = 20\,°C,\ T^*_{c,w} = -12\,°C$).

the influence of temperature variation on frost deposition when the water content in the air is kept constant. With a water content of 10 g·kg^{-1}, which is approximately equivalent to 70 % relative humidity at 20 °C, the same air temperature variation as before leads to a nearly constant mass transfer. But it can be seen that a thinner and more dense frost layer grows when the air temperature is raised. This is necessary in order to conduct the slightly increasing overall heat flux through the frost due to the increasing sensible component alone. In summary, it can be stated that for a constant water content the effect of air temperature variation on frost deposition is marginal.

4.4. Variation of wall temperature

Decreasing the wall temperature is another way to increase the maximum available concentration difference in the moist air stream. Since the change in concentration difference is small as compared to the previously dis-

cussed variation in relative humidity, the effect on mass transfer to the frost surface is modest, too. Both, the mass and the sensible heat transfer rates vary almost linearly with wall temperature, but do not vary with time. However, the overall heat transfer [18] from the air stream to the surface does not change to the same extent as the temperature gradient in the frost layer. To conduct the total heat through the porous layer, the thermal resistance has to decrease. This is achieved by reducing the thickness and the porosity with rising wall temperature. Thus, the wall temperature strongly affects the average frost height and the density. *Figure 12* shows the time variation of the frost height for different cold plate temperatures. It can be seen that the growth rate gradually weakens, since the share of water used for densification increases while the total amount available remains almost constant.

In *figure 13* the measured and predicted frost contours for different times are compared. The correspondence is very satisfactory, especially for $t^* = 60$ min, not only the height in the front part but also the slope in the rear part match fairly well.

5. CONCLUSION

Frost formation on cooled parallel plates in laminar forced convection was investigated theoretically and by experiment. A fully numerical model has been developed to predict the growth process, whereby the distribution of the surface porosity is the only parameter left to alter. On the basis of general considerations and experimental findings the porosity distribution in the frost layer has been predicted reasonably.

Air velocity, air humidity, and wall temperature are the main parameters that influence frost formation. An increase in mass transfer to the frost surface due to an increase in air velocity mainly leads to a more dense frost layer with a fairly constant thickness. An increase in air humidity always causes the frost layer to grow faster. However, the timewise variation in density is more complex. At low humidity the density decreases at first, at high humidity it continuously increases. But in the long term density always behaves proportional to the water content in the air. A reduction in plate temperature leads to a quicker and more porous frost layer growth since the amount of water available remains almost unchanged. Variation of air temperature with constant water content has only minor effect on frost formation.

The overall correspondence between the theoretical and experimental results is satisfactory. Nevertheless, some improvements are desirable, in particular, an extension of the simulation model to deal with “meltback” and measurements of the local porosity gradient.

REFERENCES

[1] Hosoda T., Uzuhashi T., Effects of frost on the heat transfer coefficient, Hitachi Review 16 (1967) 254–259.

[2] Chung P.M., Algren A.B., Frost formation and heat transfer on a cylinder surface in humid air cross flow, Parts I and II, ASHRAE Trans. 65 (1959) 213–228, 229–244.

[3] Piening W., Der Wärmeübergang an Rohren bei freier Strömung unter Berücksichtigung der Bildung von Schwitzwasser und Reif, Gesundheits-Ingenieur 42 (1933) 493–497.

[4] O’Neal D.L., Tree D.R., A review of frost formation in simple geometries, ASHRAE Trans. 90 (1985) 267–281.

[5] Padki M.M., Sherif S.A., Nelson R.M., A simple method for modeling the frost formation phenomenon in different geometries, ASHRAE Trans. 95 (1989) 1127–1137.

[6] Kamath J., Frost formation between closely spaced parallel plates, PhD Thesis, University of Michigan, USA, 1985.

[7] Mao Y., Besant R.W., Falk J., Measurement and correlations of frost properties with airflow at room temperature over a flat plate, ASHRAE Trans. 99 (1993) 739–745.

[8] Östin R., Andersson S., Frost growth parameters in a forced air stream, Internat. J. Heat Mass Transfer 34 (1991) 1009–1017.

[9] Seki N., Fukusako S., Matsuo K., Uemura S., An analysis of incipient frost formation, Wärme- und Stoffübertragung 19 (1985) 9–18.

[10] Hayashi Y., Aoki A., Adachi S., Hori K., Study of frost properties correlating with frost formation types, ASME J. Heat Transfer 99 (1977) 239–245.

[11] Brian P.L.T., Reid R.C., Shah Y.T., Frost deposition on cold surfaces, Ind. Engrg. Chem. Fundam. 9 (1970) 375–380.

[12] Jones B.W., Parker J.D., Frost formation with varying environmental parameters, ASME J. Heat Transfer 97 (1975) 255–259.

[13] Tao Y.-X., Beasant R.W., Rezkallah K.S., A mathematical model for predicting the densification and growth of frost on a flat plate, Internat. J. Heat Mass Transfer 36 (1993) 353–363.

[14] VDI-Wärmeatlas, Berechnungsblätter für den Wärmeübergang, 6 Auflage, VDI-Verlag, Düsseldorf, 1991.

[15] Auracher H., Effective Thermal Conductivity of Frost, in: Heat and Mass Transfer in Refrigeration and Cryogenetics, Hemisphere Publishing Corporation, New York, 1987, pp. 285–302.

[16] Schneider G.E., Zedan M., A modified strongly implicit procedure for the numerical solution of field problems, Numerical Heat Transfer 4 (1981) 1–19.

[17] Patankar S.V., Numerical Heat Transfer and Fluid Flow, Hemisphere Publishing Corporation, New York, 1980.

[18] Lüer A., Reifbildung an parallelen, gekühlten Platten eines mit feuchter Luft laminar durchströmten Kanals, PhD Thesis, Techn. Universität Darmstadt, 1997.